RSC Advances

PAPER

View Article Online
View Journal | View Issue

Cite this: *RSC Adv.*, 2016, **6**, 93180

Quantitative measurements of charge carrier hopping transport properties in depleted-heterojunction PbS colloidal quantum dot solar cells from temperature dependent current–voltage characteristics

Andreas Mandelis,*[ab] Lilei Hu[b] and Jing Wang[a]

Received 10th September 2016
Accepted 20th September 2016

DOI: 10.1039/c6ra22645k

www.rsc.org/advances

Non-conventional (anomalous) current–voltage characteristics are reported with increasing frequency for colloidal quantum dot-based (CQD) solar cells. The causes of S-shaped or negative-exponential *J–V* curves are not well understood. Many attempts made to explain these behaviors do not fully consider the physical electronic transport processes inside the solar cell within a hopping exciton and/or dissociated charge carrier framework. In this paper physical optoelectronic processes in heterojunction PbS CQD solar cells exhibiting anomalous *J–V* characteristic curves which are likely to share common origins with other QD solar cells with similar *J–V* characteristics are studied at 300 K, 250 K, 200 K, 150 K and 100 K and a suitable theoretical model of purely hopping transport is developed. Hopping exciton-dissociation-generated hole accumulation at, and near, the CQD/metal interface leading to a space-charge layer (SCL) of temperature-dependent width is predicted, and a new "hopping" Einstein relation is derived and experimentally demonstrated. A two-diode-equivalent charge carrier transport model is invoked and quantitative measurements of hopping carrier transport parameters are made both in the forward region and the reverse SCL, based on the *J–V* characteristics at those temperatures. The quantitative results add physical insight to the transport mechanism in glass/FTO/TiO_2/PbS QD/MoO_3/Au/Ag solar cells, in the bulk CQD film as well as within the SCL. These insights can be used for potential design improvement to maximize solar power conversion efficiencies, such as optimal dot-to-dot distance for maximizing charge carrier diffusivity and mobility.

1 Introduction

Most colloidal quantum dot (CQD) solar cells can be categorized into Schottky-junction, heterojunction and CQD sensitized solar cells. They exhibit exponential Shockley-type *J–V* characteristics at room temperature.[1–6] However, anomalous *J–V* characteristics have been reported for several types of CQD solar cells and mainly encountered in organic solar cells. They are widely known as S-shaped *I–V* characteristics. For example, Wang *et al.*[7] obtained S-shaped *J–V* curves in bilayered heterojunction organic solar cells, which were attributed to electron accumulation effects induced by an exciton blocking layer. Wagenpfahl *et al.*[8] focused on effects of metal–semiconductor interfaces and qualitatively considered the reduction of hole-associated surface recombination velocities (SRV). Zuo *et al.*[9] studied the *J–V* S-shape dependence on various anode buffer layers in Schottky junctions. Romero *et al.*[10] developed equivalent electric circuit models that can qualitatively simulate these kinds of *J–V* curves in terms of forward and reverse diodes, but did not consider the physical electronic transport processes inside the solar cell. In summary, the origins of S-shaped or negative-exponential *J–V* curves are not well understood. In the literature, several potential reasons have been suggested: interfacial dipoles, charge accumulation at the CQD–metal interface, unbalanced charge transport, and electrode/active layer interfacial Schottky barriers.[11–14] Although *J–V* anomalies might originate due to different reasons, the shapes of reported *J–V* curves show consistent similarities which indicate a possible common physical basis of these effects. Such studies have not been reported, especially for CQD solar cells, to the best of our knowledge, yet, they are important because, with interface optimization, solar cells can exhibit improvements in power conversion efficiency.[15]

While room temperature characterization is not sufficient to reveal charge carrier transport in CQD systems, yet, a thorough understanding of *J–V* characteristics is essential for solar cell

[a]*School of Optoelectronic Information, University of Electronic Science and Technology of China, Chengdu, Sichuan, 610054, China. E-mail: mandelis@mie.utoronto.ca*
[b]*Center for Advanced Diffusion-Wave and Photoacoustic Technologies (CADIPT), Department of Mechanical and Industrial Engineering, University of Toronto, Toronto M5S 3G8, Canada*

optimization. Detailed quantitative studies in CQD solar cells require low temperature measurements for identification of the physical processes involved in the transport. For such optimization, the effects of a Schottky barrier at the p-type PbS CQD/hole extraction contact interface must be better understood. They become more pronounced and can be more easily quantified at low temperatures, shedding light on the role of key carrier transport parameters and yielding physical insights about the origin and extent of the space charge layer (SCL) due to hole accumulation at the Schottky barrier, whence the need for low-temperature *J–V* investigations.

Conventional exponential *J–V* curves were found in this work when measured at 300 K, while negative exponential *J–V* curves were observed at low temperatures (*i.e.* 250 K, 200 K, 150 K and 100 K). Negative-exponential *J–V* curves exhibited by CQD solar cells cannot be modeled with the use of a conventional electric circuit of a single-diode coupled with a series and a shunt resistor.[16] In this work, physical optoelectronic processes in heterojunction PbS CQD solar cells exhibiting anomalous *J–V* characteristic curves which are likely to share common origins with other QD solar cells with similar *J–V* characteristics, are discussed and a suitable theoretical model of hopping transport is developed. Furthermore, the important issue of hopping transport across the QD ensemble within a colloidal medium, rather than treating exciton and dissociation-generated electron and/or hole transport with conventional continuous semiconductor band structures, is addressed. First-principles equations are developed which govern the hopping motion of excitons or the carriers emerging from their dissociation in the nanolayer bulk and within the SCL near the metal interface, leading to a new hopping Einstein relation. Quantitative measurements of hopping transport parameters in the CQD nanolayer bulk and at the CQD/metal interface SCL were made based on *J–V* characteristics at the aforementioned temperatures which can be used for potential design improvement to maximize solar power conversion efficiency.

2 Hopping transport theory in colloidal quantum dot ensembles

2.1 Hopping transport equations and parameters: mobility and diffusivity

Many controversial practices are encountered in the literature regarding the physical nature of exciton-mediated electrical transport in colloidal quantum dot materials and devices. Many authors have invoked diffusion and drift principles *ad hoc*[17–20] which are normally valid for continuous semiconducting material lattices with well-defined band structures, ignoring the conditions of carrier localization within a quantum dot and the effects of disorder which also induces *e.g.* Anderson localized electrons.[21] In an in-depth analysis of physical issues arising with respect to electrical transport in colloidal quantum dots, Guyot-Sionnest[22] concluded that *"Many separate sources of disorder make it extremely unlikely that QDS based on colloidal assemblies are anywhere close to exhibiting band-like transport behavior"*. In colloidal quantum dot (CQD) ensembles the evidence of low dot-to-dot transmission due to variations in confinement energy, electron–electron repulsion, and variations in coupling and thermal broadening points to hopping conductivity and diffusivity.[22,23]

When excitons are generated optically, they diffuse for a certain statistical diffusion length, which depends on the specific exciton lifetime. They dissociate into free electrons and holes during their interdot hopping process. It is difficult to precisely identify where and when dissociation occurs during the transport process. Therefore, three types of charge carriers in a CQD solar cell will be considered: electrons, holes, and excitons. Despite the different physical transport processes, given the equivalence of effects of electric fields on exciton transport, most likely through dipole coupling,[24–26] and those of hopping transport of the exciton dissociation-generated carriers, the proposed theory is applicable to both excitons and free carriers with proper definitions of transport parameters in each case. Therefore, for CQD solar cells (and for coupled PbS CQD solar cells in particular), a mathematical foundation based on hopping transport rate equations consistent with the discrete nature of electrical transport is necessary for an improved understanding of the operating charge transport processes across these devices. In the remainder of this section, a hopping-transport-based drift current density model for QD solar cells will be derived from first-principles. Simultaneous excitonic and dissociated charge carrier hopping diffusion due to population gradients is considered. In summary, owing to its first-principles kinetic approach, the particle density-flux formalism derived from the exciton hopping transport model also holds for the exciton-dissociation-generated carrier hopping current densities within the bulk of the colloidal thin film following dissociation, and within the SCL adjacent to the CQD/metal interfaces.

For a one-dimensional (1D) ensemble of quantum dots each separated by a mean distance from its nearest neighbors and characterized by its own size and energy manifold, the rate equation for the particle population $N_i(x,t)$ [particles per cm^3] in quantum dot (i) is given as the net rate of particles hopping in and out of the quantum dot[27]

$$\frac{\partial N_i(x,t)}{\partial t} = -\frac{N_i(x,t)}{\tau} - \sum_j P_{ij} N_i(x,t) + \sum_j P_{ji} N_j(x,), \qquad (1)$$

where P_{ij} is the probability for a particle to migrate from a quantum dot (i) to quantum dot (j), and τ is the total lifetime of the particle (limited by dissociation for excitons and recombination for charge carriers). For a 1D flow of particles hopping in and through a virtual volume element $\mathrm{d}V = A\mathrm{d}x$ of the colloidal medium, the net flux $J_e(x,t)$ [particles per cm^2 s] across a cross-sectional area A, Fig. 1(a), is given by

$$A[J_e(x,t) - J_e(x+\mathrm{d}x,t)]\mathrm{d}t = -\frac{\partial}{\partial x} J_e(x,t)\mathrm{d}V\mathrm{d}t \qquad (2)$$

The net particle population rate entering $\mathrm{d}V$ in the time interval $\mathrm{d}t$ is found from eqn (1) and (2)

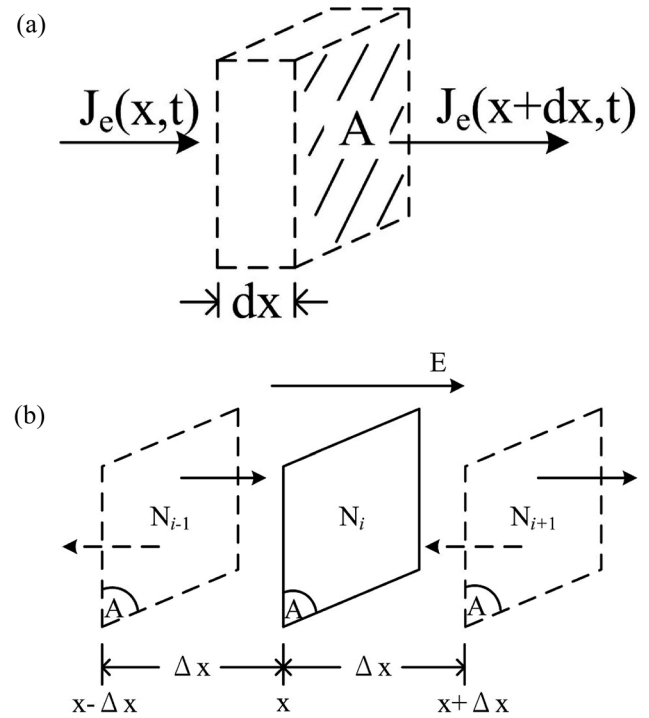

Fig. 1 (a) Virtual volume element $dV = Adx$ for hopping exciton/charge carrier ("particle") transport equation and parameter derivation in a QD medium. $J_e(x,t)$ [particles per cm^2 s] is the incident particle flux. (b) Schematic of particle kinetic flux into a virtual plane (i) from adjacent planes ($i-1$) and ($i+1$), all of area A across the thickness direction of a CQD solar cell.

$$\frac{\partial N_i(x,t)}{\partial t} = -\frac{\partial J_e(x,t)}{\partial x} - \frac{N_i(x,t)}{\tau}, \tag{3}$$

where the first term on the rhs represents trans-volume particle hopping into (entering) and/or out of (leaving) dV, and the second term accounts for local particle de-excitation within dV. The exact calculation of the summation terms over the entire ensemble of particles in eqn (1) is very difficult, so the nearest neighbor hopping (NNH) approximation will be adopted. Fig. 1(b) shows the kinetics of NNH in 1D. In the presence of a particle population gradient (*e.g.* due to external optical excitation), the net flux $J_e(x,t)$ at the quantum dot (QD) (i) consists of contributions from fluxes out of quantum dots ($i+1$) and ($i-1$) into the quantum dot (i). These fluxes are:

$$\begin{aligned} J_{i+1,\mathrm{in}}(x+\Delta x,t) &= \frac{1}{2}N_{i+1}(x+\Delta x,t)f_{i+1}e^{-\gamma\Delta x} \\ J_{i-1,\mathrm{in}}(x-\Delta x,t) &= \frac{1}{2}N_{i-1}(x-\Delta x,t)f_{i-1}e^{-\gamma\Delta x} \end{aligned} \tag{4}$$

Here, the factor $\frac{1}{2}$ denotes the equal probabilities for an exciton in QD_i to hop into QD_{i+1} (right) and QD_{i-1} (left) in 1D geometry. The factors f_j and $e^{-\gamma\Delta x}$ denote particle hopping (attempt) frequencies and the quantum dot-to-quantum dot crossing probability, with γ being the hopping transmission coefficient to the NN QD. Invoking particle flux conservation, the net flux across the virtual area A at x is

$$\begin{aligned} J_i(x,t) &= J_{i-1,\mathrm{in}}(x-\Delta x,t) - J_{i+1,\mathrm{in}}(x+\Delta x,t) \\ &= \frac{1}{2}e^{-\gamma\Delta x}\left[\frac{N_{i-1}(x-\Delta x,t)}{\tau_{\mathrm{h},i-1}} - \frac{N_{i+1}(x+\Delta x,t)}{\tau_{\mathrm{h},i+1}}\right]\Delta x \end{aligned} \tag{5}$$

where $\tau_{h,j} = 1/f_{h,j}$ is the hopping time from/to QD_j which is different for attempts in the direction of, and opposite to, the population gradient. A particle hopping velocity $v_{h,j}$ from/to QD_j can be introduced by letting $\Delta x = L = v_{h,j}\tau_{h,j}$ with L being the effective QD-to-QD distance. In the presence of an external or internal electric field E, the overall velocity will include an induced drift velocity, $v_{dr,h}$, for both dissociated carriers and quasi-neutral excitons (j) affected by the electric field:

$$v_{T,j} = v_{h,j} \pm v_{dr,j} \tag{6a}$$

Dissociated carriers (charge q) are affected by the attractive, $j = i-1$, and repulsive, $j = i+1$, electric field-E-induced force, respectively. Considering the charge carrier's kinetic energy in the limit of a weak electric field, it can be shown from eqn (4) and (5) that the hopping velocity, $v_{h,j}(E)$, in the presence of the electric field E is related to the hopping velocity, $v_{h,j}(0)$, without the field:

$$v_{h,i\pm1}(E) = v_{h,i\pm1}(0) \pm \frac{qEL}{m_{ex}v_{h,i\pm1}(0)} \tag{6b}$$

Here, m_{ex} is the effective particle mass and the $\pm$ signs denote motion in the direction (+) or opposite to the direction (−) of the electric field vector. In the case of quantum dot excitons, Hönig *et al.*[26] have shown that an electric field E changes the dipole moment $\vec{p} = q\vec{R}$ of an exciton of effective length R between the constituent electron and hole along the direction of the field, which impacts its potential energy $\Delta U_{pot} = \Delta\vec{p}\cdot\vec{E}$. This mechanism implies that the length R is stretched or shrunk in the presence of the electric field depending on direction and angle between the two vectors: $\Delta\vec{p} = \pm q\Delta\vec{R}$. The net effect of the electric field is an effective motion (drift) of the exciton with the peak drift velocity in the direction of the electric field

$$v_{dr,j} = \left(\frac{2\Delta U_{pot}}{m_{ex}}\right)^{1/2} = \left[\frac{2E(\mathrm{d}\vec{p}/\mathrm{d}E)\cdot\vec{E}}{m_{ex}}\right]^{1/2} \tag{6c}$$

where $d\vec{p}/dE$ is the gradient of the exciton dipole moment in the electric field, a physical property of the quantum dot medium. Eqn (6c) can be used to define an effective exciton mobility

$$\mu_{ex} = \sqrt{\frac{2(\mathrm{d}\vec{p}/\mathrm{d}E)\cdot\hat{n}_E}{m_{ex}}} \tag{7a}$$

where $\hat{n}_E$ is a unit vector in the direction of the electric field. For very close NNH distances (~1 nm), expanding the $N_{i\pm1}(x\pm\Delta x)$ terms in eqn (5) and retaining the first (linear) order terms yields for both excitons and dissociated carriers

$$J_i(x,t) \approx \left[-v_{h0}L\left(\frac{\partial N_i(x,t)}{\partial x}\right) + v_{dr,i}N(x,t)\right]e^{-\gamma L} \tag{7b}$$

Here, $v_{h0} \equiv v_{h,i}(0)$. This expression can represent the net flux of both excitons and carriers generated from exciton dissociation.

It can be compared with that for conventional p-type carrier transport (p-type transport is also the case with PbS depleted heterojunction CQDs) in continuous semiconductors.[28] A similar expression is used for nanocrystalline and QD media[17,29]

$$J(x,t) = -D\left[\frac{\partial N(x,t)}{\partial x}\right] + \mu_e E N(x,t) \quad (8)$$

It is immediately recognized that the first term on the rhs of eqn (7b) is related to hopping diffusion with diffusivity

$$D \equiv D_h(T) = \left(\frac{L^2}{\tau_h(T)}\right)\exp(-\gamma L) \quad (9)$$

The second term is associated with hopping drift in the presence of an external or internal electric field. When excitons are involved, the hopping mobility is given by

$$\mu_{ex,h}(T) = \mu_{ex}(T)\exp(-\gamma L) \quad (10a)$$

with $\mu_{ex}(T)$ given by eqn (7a). When exciton dissociation carriers are involved, eqn (6b) yields

$$\mu_{e,h}(T) = \left[\frac{qL}{m_e v_{h0}(T)}\right]\exp(-\gamma L) \equiv \mu_e(T)\exp(-\gamma L) \quad (10b)$$

Eqn (10a) and (10b) are very similar in their structure. The part that differs is the mechanism of interaction with the electric field. In eqn (9) and (10) there are additional activation-energy mediated temperature dependencies which need to be added because they are relevant to the experimental investigations in this work. If inter-quantum-dot hopping is an exponentially thermally activated process, the time constant defining the hopping diffusivity in eqn (9) is linked to the probability P_{ij} in eqn (1) and is given by[27]

$$\frac{1}{\tau_h(T)} = \left(\frac{1}{\tau_0}\right)\exp(-\Delta E_{ji}/kT) \quad (11a)$$

Here, ΔE_{ji} is the energy difference of a hopping particle in quantum dot state (i) (initial) and (j) (final): $\Delta E_{ji} = E_j - E_i \geq 0$; it depends on the relative size (and size homogeneity across the CQD medium) and its energy state manifold. Henceforth, for simplicity we will set $\Delta E_{ji} \equiv \Delta E$. The quantity τ_0 is a characteristic time for tunneling of particles between nearest neighbor quantum dots at a distance x. It is temperature independent and given by[27]

$$\frac{1}{\tau_0} = f\,\exp(-\gamma_{ij}\Delta x_{ij}) \quad (11b)$$

where f is an attempt frequency and γ_{ij} is related to the tunneling probability across the energy barrier of effective thickness/distance Δx_{ij} that separates the two quantum dots at locations (i) and (j). γ_{ij} and Δx_{ij} have been symbolized as γ and L in eqn (7), (9) and (10). Eqn (10a) and (10b) concern drift due to local electric fields, as opposed to hopping diffusion. Major mechanisms affecting local electric fields have been identified to be disorder in energy levels, electron–electron repulsion in small quantum dots, and disorder in the coupling between particles.[22] Guyot-Sionnest has proposed the following expression for the carrier mobility in the bulk of a CQD

$$\mu(T) = \left(\frac{qL^2E_a}{3hkT}\right)\exp(-\gamma L - E_a/kT) \quad (12)$$

where h is Planck's constant and E_a is the sum total of the energy barriers encountered by the hopping particle. This expression is structurally similar to eqn (10a) and (10b), but for the thermal process with activation energy E_a estimated to be in the range of 10–50 meV.[22] This magnitude is consistent with experimental results in this work. The foregoing discussion elucidates differences in the activation energies limiting hopping diffusion *vs.* drift mechanisms in quantum dot layers: both transport processes are spatially limited by dot-to-dot tunneling; diffusion is further thermally limited by NN quantum dot energy state differences, and dissociated carrier drift is due to the presence of local electric fields. For excitons, drift is controlled by dipole moment gradient coupling to the local electric field which occurs at very short dot-to-dot distances,[22] and is also a result of exciton–phonon scattering which causes the local exciton density to fluctuate.[23]

Granero *et al.*[17] used conventional continuous energy band carrier transport equations to describe excitonic transport in periodical interdigitated organic solar cells, and derived an excitonic diffusivity $D_{exc} = L^2/\tau$ where L is the exciton diffusion length and τ is the exciton mean lifetime. Clearly, in the hopping picture, a very different physical interpretation with respect to diffusivity, critical transport length, and the physics of exciton transport has emerged. Two major immediate consequences arise:

(1) Temperature dependent charge carrier accumulation at, and near, the interface, with a resultant emergence of a "built-in" electric field and an accumulation layer opposing the further flow of charge carriers of the same type across the junction. This is a reverse Schottky barrier predicted for CQD solids by the hopping conduction theory, the hopping carrier transport equivalent to the conventional semiconductor band-bending. In the immediate neighborhood of the CQD–metal junction interface, the externally measured mobility due to dissociated exciton carriers assumes the form

$$\mu_{ext\,i}(T) = \left(\frac{qL}{m_e v_{h0}(T)}\right)\exp[-\gamma_i L - (E_{ai}/kT)] \quad (13a)$$

where E_{ai} is the local energy barrier within the charge accumulation layer (the SCL). The temperature dependence of the bulk mobility outside the SCL can be re-defined from eqn (12) as

$$\mu_{ext}(T) = \left(\frac{A_1}{T}\right)\exp(-\gamma L - E_a/kT) \quad (13b)$$

where A_1 is a temperature independent constant. The CQD-metal interface activation energy E_{ai} amounts to a Schottky barrier that has to be overcome by free-carriers adjacent to the junction which must clear the barrier thermally.

(2) The breakdown of the conventional Einstein relation used in semiconductor carrier transport. In view of eqn (9),

(10a), (11a) and (12), the ratio of mobility to diffusivity now takes on the "hopping" activation form in the bulk of the CQD:

$$\frac{\mu_{ext}(T)}{D_h(T)} = \left(\frac{q\tau_0 E_a}{3hkT}\right)\exp[-(E_a - \Delta E)/kT] \equiv \left(\frac{A_2}{T}\right)\exp\left(-\frac{\Delta E_a}{kT}\right) \quad (14)$$

where $\mu_{ext} = \mu_{ex,h}$ is the bulk mobility in eqn (10a) or (10b) as measured in the external circuit. It can be seen that the conventional Einstein relation can be obtained in the case $E_a = \Delta E = h/\tau_0$, *i.e.* when the diffusion and drift rates are limited by the same thermal activation process (defined as thermal velocity in continuous band semiconductors) and the rate-limiting step is the dot-to-dot tunneling rate τ_0^{-1}. An Einstein relation similar to eqn (14) with the net activation energy $\Delta E_{ai} = E_{ai} - \Delta E_i$ is assumed to be valid within the charge accumulation layer, a hypothesis that was subsequently verified experimentally.

2.2 Current density $J(x)$ across the CQD nanolayer

Following exciton dissociation, free electron and hole carriers reach the TiO_2/PbS CQD and PbS CQD thin film/MoO_3 interfaces. In the bulk PbS CQD thin films, in competition with intrinsic radiative and nonradiative recombinations, excitons dissociate *via* phonon-assisted hopping to their NN, or are split up by the intrinsic electric field in the device depletion regions.[30] As already mentioned, the theoretical hopping transport model derived in Section 2.1 is applicable to electron and hole kinetics within the SCL and at the interface region. In the energy diagram of a TiO_2/CQD/MoO_3/Au/Ag solar cell,[2] Fig. 2(a), eqn (7b) is applied at equilibrium with $J_i(x,t) = 0$ across the solar cell thickness d

$$D_h(T)\frac{dN(x)}{dx} - \mu_{ext}(T)EN(x) = 0; \quad 0 \le x \le d \quad (15)$$

The subscript (i) has been dropped as the discrete spatial location is adequately represented by the coordinate variable x. Using $E(x) = -\frac{dV(x)}{dx}$ and integrating over the thickness of the solar cell yields the equilibrium relation

$$\frac{N(0)}{N(d)} = \exp\left(-\frac{\mu_{ext}V_0}{D_h}\right); \quad V_0 \equiv V(0) - V(d) \quad (16)$$

For the non-equilibrium case where a forward bias photovoltage V_a is generated due to differences in work function between the front and back contacts upon illumination of the CQD medium, leading to excess free carrier population, eqn (16) can be modified directly

$$\frac{N_{PV}(0)}{N_{PV}(d)} = \exp\left[-\frac{\mu_{ext}}{D_h}(V_0 - V_a)\right] \quad (17)$$

Defining the excess charge carrier population on the illuminated surface as $\Delta N_{PV}(0) = N_{PV}(0) - N(0)$ and assuming a quenching boundary condition at $x = d$,[18,20] eqn (16) and (17) yield

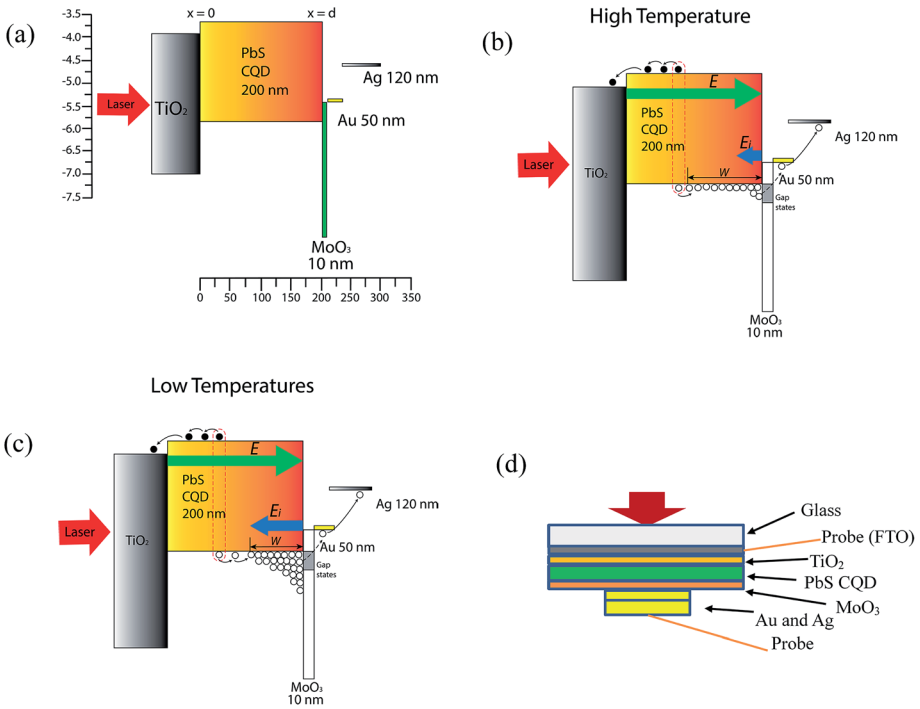

Fig. 2 (a) CQD solar cell band-energy-equivalent structure. (b) Room temperature and (c) low temperature hole accumulation at the PbS CQD–MoO_3 interface, also showing transport across the junction. (d) Solar cell architecture from top to bottom: laser beam, glass/FTO (back contact)/TiO_2/PbS CQD/MoO_3/Au/Ag (front contact).

$$\Delta N_{PV}(0) = N_{PV}(0)\left[\exp\left(\frac{\mu_{ext}V_a}{D_h}\right) - 1\right] \quad (18)$$

The main features of this Shockley-type expression of relevance to this investigation are (a) it is valid regardless of the specific functional dependence of $N_{PV}(x)$ on the depth coordinate; (b) the conventional Einstein relation has not been used to replace the ratio of mobility to diffusivity in the exponent, as per the discussion leading to eqn (14); (c) even if the quenching boundary condition is not valid, the correction is the multiplicative ratio $N_{PV}(d)/N(d)$. For ultrathin CQD layers the number of photons absorbed across the thickness of the layer is relatively small, so the ratio replaces $N_{VP}(0)$ with $N_{PV}(d) \approx N_{PV}(0)$. Under dc illumination the current density, eqn (7), must be inserted in the steady-state form of the rate eqn (3):

$$\frac{d^2N_{PV}(x)}{dx^2} - \left[\frac{\mu_{ext}(T)E}{D_h(T)}\right]\frac{dN_{PV}(x)}{dx} - \frac{N_{PV}(x)}{D_h(T)\tau(T)} = 0 \quad (19)$$

Here, $\tau(T)$ represents the total lifetime of the charge carrier. The solution is

$$N_{PV}(x) = A\, e^{Q_1 x} + B\, e^{Q_2 x},$$

where

$$Q_{1,2}(T) \equiv \frac{1}{2}\left(C_0 \pm \sqrt{C_0^2 + 4C_1}\right) \equiv \frac{1}{2}(C_0 \pm \Delta) \quad (20)$$

The surface/interface recombination velocity S_i is finite if the accumulation opposes the flow of free (hopping) charges across the interface. This is the source of the interfacial built-in electric field, E_i, in the opposite direction of E, the forward electric field generated across the thin film due to the photovoltage. The resulting equation for the excess charge carriers is

$$\Delta N_{PV}(x) = \Delta N_{PV}(0)\left[\frac{(S_i + D_h Q_1)e^{Q_1 d + Q_2 x} - (S_i + D_h Q_2)e^{Q_2 d + Q_1 x}}{(S_i + D_h Q_1)e^{Q_1 d} - (S_i + D_h Q_2)e^{Q_2 d}}\right] \quad (23)$$

The following equations for the exponents are shown in terms of the defined parameters C_0 and Δ:

$$\begin{aligned} Q_1 d + Q_2 x &= \frac{1}{2}C_0(d + x) + \frac{1}{2}\Delta(d - x) \\ Q_2 d + Q_1 x &= \frac{1}{2}C_0(d + x) - \frac{1}{2}\Delta(d - x) \end{aligned} \quad (24)$$

Separating out the current densities into hopping diffusion and drift components consistent with eqn (7), using eqn (18) and (23) and highlighting the temperature dependence gives

$$J_e(0,T) = J_{e,diff}(0,T) + J_{e,drift}(0,T)$$

with

$$J_{e,diff}(0,T) = N_0\left(\exp\left[\frac{\mu_e(T)V_a}{D_h(T)}\right] - 1\right)D_h(T) \times \left[\frac{-Q_2(T)\{S_i(T) + D_h(T)Q_1(T)\}e^{\Delta d/2} + Q_1(T)\{S_i(T) + D_h(T)Q_2(T)\}e^{-\Delta d/2}}{\{S_i(T) + D_h(T)Q_1(T)\}e^{\Delta d/2} - \{S_i(T) + D_h(T)Q_2(T)\}e^{-\Delta d/2}}\right] \quad (25a)$$

with the definitions

$$\begin{aligned} &C_0(T) \equiv \frac{\mu_{ext}(T)E}{D_h(T)};\quad C_1(T) \equiv \frac{1}{L_h^2(T)}; \\ &L_h(T) = \sqrt{D_h(T)\tau(T)};\quad \Delta \equiv \sqrt{C_0^2 + 4C_1} \end{aligned} \quad (21)$$

$L_h(T)$ is the hopping diffusion length. The constants A and B can be found subject to (a) an illuminated surface boundary condition at $x = 0$: $N_{PV}(0) = N_0$ determined by the photon flux irradiating the surface of the solar cell; and (b) a hole accumulation boundary condition at $x = d$. For the hopping charge carrier flux across the back interface in the presence of a reverse Schottky barrier, this boundary condition arises due to hole accumulation at the PbS–MoO_3 boundary, Fig. 2(b) and (c), and can be written as:

$$-D_h(T)\left.\frac{dN_{PV}(x)}{dx}\right|_{x=d} = S_i(T)N_{PV}(d) \quad (22)$$

and

$$J_{e,drift}(0,T) = N_0\left(\exp\left[\frac{\mu_e(T)V_a}{D_h(T)}\right] - 1\right)\mu_{ext}(T)E; \quad 0 \le x \le d \quad (25b)$$

3 Solar cell fabrication and J–V measurements

Coupled thin films with average PbS CQD diameter of 4.2 nm were fabricated through a layer-by-layer process in which the long oleic acid ligands were displaced by shorter 3-mercaptopropionic acid ligands resulting in an inter-particle spacing *ca.* 0.5–1 nm.[2] The device architecture was[1] glass/FTO/TiO_2/PbS QD/MoO_3/Au/Ag, Fig. 2(d). For our CQD solar cells, a very thin 10 nm hole extraction layer of MoO_3 was deposited between the anode Au and PbS CQD layer, Fig. 2.[1] Mechanisms of hole extraction, such as through a dipole formed at the interface between organic photovoltaic cell active transport layers and the

respective anodes, have been proposed[3,31,32] featuring carrier transport through deep-lying conduction band or gap states in MoO_3.

For *J–V* characteristics, A 30 mW CW diode laser with wavelength 830 nm and a beam diameter of *ca.* 0.1 mm was used as the excitation and photovoltage generation source. A variable resistor was connected as a load resistance in the range from 0 to 99 MΩ. The sample was placed on a Linkam LTS350 cryogenic stage, which allows maintaining a constant temperature in the 77–520 K range. The *J–V* responses of the CQD solar cells were tested at various temperatures (100 K, 150 K, 200 K, 250 K, and 300 K). The resulting *J–V* characteristics are shown in Fig. 3(b)–(f).

4 Results and discussion

4.1 Structural origin of S-shaped *J–V* characteristics

Fig. 3(b)–(f) show that the *J–V* characteristic curves are only exponential at 300 K. Negative exponential shapes are obvious at all other (lower) temperatures. Turning attention to the CQD–MoO_3 interface, in addition to its interfacial hole-transport-related action, this nanolayer has been known to affect the shape of the *J–V* curves of CQD solar cells, giving rise to non-exponential curves. Consistent with the aforementioned reports, Chuang *et al.*,[3] found that CQD solar cells with MoO_3 nanolayers exhibited S-shaped *J–V* curves and low stability, while devices without the MoO_3 layer exhibited better performance and normal *J–V* curves. The MoO_3 layer's deep-level conduction band and gap states can be the result of improper stoichiometry, or ambient air/water molecule adsorption–absorption effects, or different deposition conditions during the fabrication process.[33,34] This, however, can result in accumulation of holes at the PbS CQD–MoO_3–Au back interface, as anticipated in the theory of Sect. 2. In view of the deep or shallow gap states in MoO_3, and the hopping transport nature of holes across the CQD layer–MoO_3–Au interface, a trap- and phonon-assisted hopping transport mechanism can be invoked. The latter is known to occur in excitonic hopping in some doped crystals[35] where the low phonon population at low temperatures results in low hopping rates. Therefore, Fig. 3(a) proposes a composite diode model, comprising a forward diode to account for the TiO_2/PbS CQD heterojunction diode, Section 2.2, and including a superposed second (reverse Schottky) diode that arises naturally from the charge accumulation effect induced at the interface by inserting the MoO_3 layer and the effective Schottky barrier E_{sc}. The transport properties of the two diodes such as hopping diffusivity and mobility are expected to be different and are extracted from the application of the hopping theory to the two-diode model.

4.2 Two-diode-equivalent current density transport model

In the diagram of Fig. 2(b) and (c), any hole accumulation at the CQD film–MoO_3 interface due to the effective energy barrier to holes originating in the 10 nm MoO_3 and the 50 nm metallic Au overlayer, will give rise to a local space charge layer (SCL) of width W and a built-in electric field directed toward the bulk of the thin CQD film. This SCL acting as a reverse Schottky diode will modify the diffusion and drift current densities of eqn (25) by introducing opposing currents within the SCL width. The hole accumulation SCL is superposed on a fraction of the thickness d starting at the back boundary. Letting $N_{PV}(d - W) = N_0$, a reasonable assumption based on the extreme thinness of the CQD nanolayer which results in very small attenuation of the incident photon flux due to absorption, and retaining the back interface boundary condition eqn (22), it can be shown that

$$J_{ei,\mathrm{diff}}(d-W,T) = N_0\left(\exp\left[\frac{\mu_{\mathrm{ext}\,i}(T)V_{ai}}{D_{\mathrm{h}i}(T)}\right]-1\right)D_{\mathrm{h}i}(T) \times\left[\frac{-Q_{2i}(T)\{S_i(T)+D_{\mathrm{h}i}(T)Q_{1i}(T)\}\mathrm{e}^{\Delta_i(d-W)/2}+Q_{1i}(T)\{S_i(T)+D_{\mathrm{h}i}(T)Q_{2i}(T)\}\mathrm{e}^{-\Delta_i(d-W)/2}}{\{S_i(T)+D_{\mathrm{h}i}(T)Q_{1i}(T)\}\mathrm{e}^{\Delta_i(d-W)/2}-\{S_i(T)+D_{\mathrm{h}i}(T)Q_{2i}(T)\}\mathrm{e}^{-\Delta_i(d-W)/2}}\right]; \quad (26a)$$

and

$$J_{ei,\mathrm{drift}}(d-W,T) = -N_0\left(\exp\left[\frac{\mu_{\mathrm{ext}\,i}(T)V_{ai}}{D_{\mathrm{h}i}(T)}\right]-1\right)\mu_{\mathrm{ext}\,i}(T)|E_i|; \quad d-W\le x\le d \quad (26b)$$

Here the transport parameters have taken on local values (i). The built-in field E_i opposes the work-function-difference-induced field E, Fig. 2(b) and (c), and increases with hole accumulation at the back interface. Its carrier-flux-impeding effect is expected to become more pronounced with decreasing diffusivity and mobility and increased hole accumulation at decreasing temperatures, and with increasing effective Schottky barrier height, ΔE_a. At first glance, this is qualitatively borne out in the *J–V* characteristics by the significant decrease in current density J with decreasing temperature. There is no upper limit to the extent of the accumulation layer width W other than the entire thickness of the CQD layer. The physical picture involving eqn (25) and (26) is one of hopping conduction occurring simultaneously across the thickness of the CQD layer (forward direction) and across the hole accumulation SCL (reverse direction) with the net carrier (hole) current being the superposition of both carrier motions. The SCL width is effective and it should not be considered as acting like an interface boundary to distinguish the heterojunction diode and the reverse Schottky diode. The values obtained from applying the theory to the data are

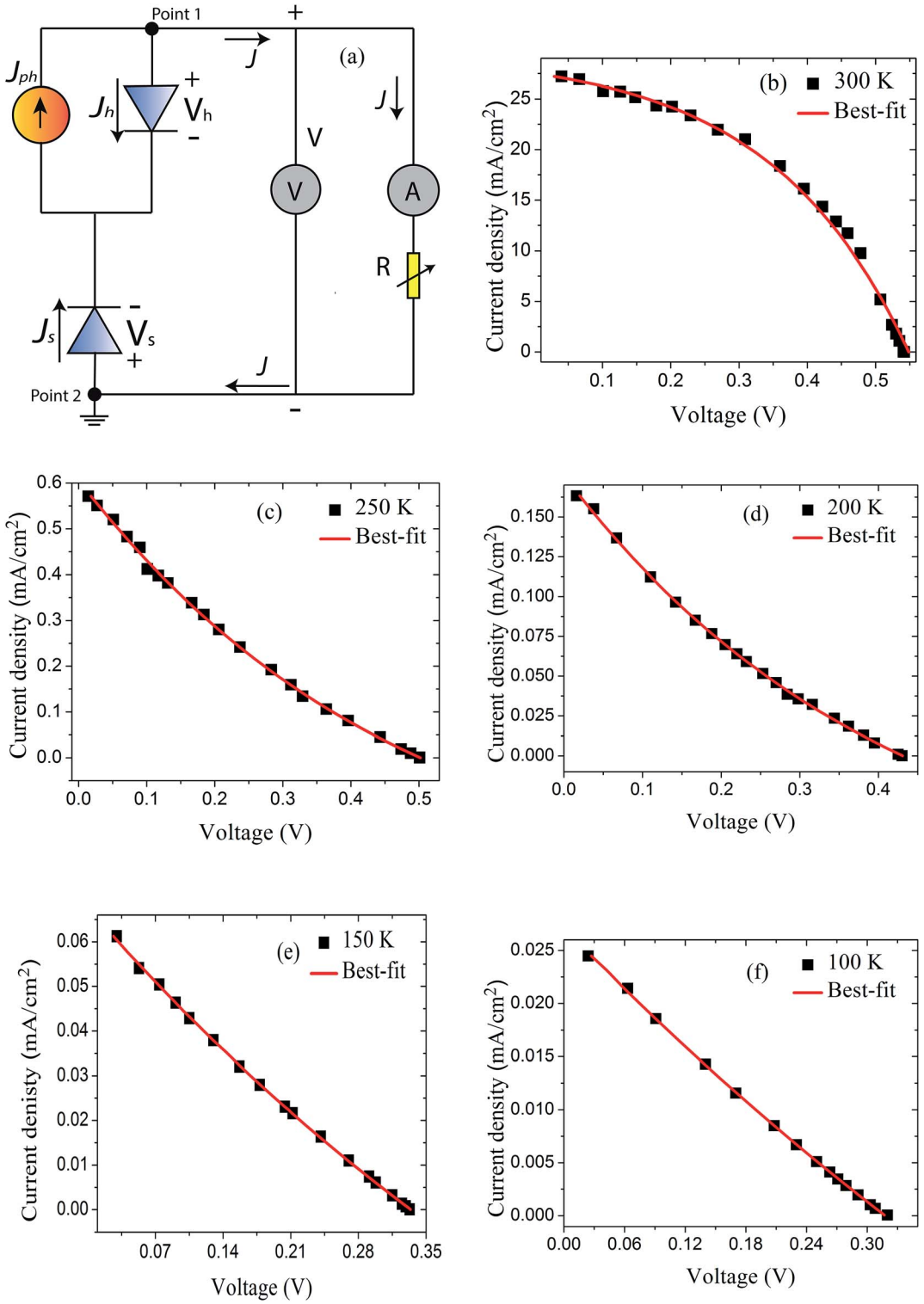

Fig. 3 (a) Experimental set-up for J–V measurement as well as the two-diode electric circuit model of the TiO_2/PbS QD/MoO_3/Au solar cell. (b)–(f) Current–voltage characteristic curves of solar cell architecture: glass/FTO/TiO_2/PbS QD/MoO_3/Au/Ag obtained at 100 K, 150 K, 200 K, 250 K and 300 K. Continuous lines: best fits to data using eqn (35).

actually nominal numbers which can be equal to the solar cell thickness. The SCL width is defined only for the purpose of using it to adjust the electric field strength. Given that the electric field in the SCL region is inversely proportional to the SCL width, when the nominal value of the latter is ~200 nm, this physically indicates that holes are diffused across the entire layer thickness d with an extremely small concentration gradient which results in a very weak electric field strength,

consistent with the *J–V* curve at 300 K. Note that if the SCL width $W = d$, eqn (26b) for the electric field-induced drift current reduces to eqn (25b), meaning there is no reverse electric field.

From the composite diode model of Fig. 3(a) the following circuit analysis can be made: At circuit points 1 and 2, respectively, the photocurrent, external (measured), and reverse diode current are related through

$$J_{ph}(0,T) = J(T) + J_h(T) \tag{27a}$$

$$J(T) = J_s(T) \tag{27b}$$

It is generally true that $J_h(T)$ and $J_s(T)$ include both diffusion and drift current components. However, $J_h(T)(J_s(T))$ is mainly contributed by the majority charge carrier electrons (holes) in the heterojunction (Schottky) diode.

The voltage across the circuit is the superposition of the two opposing voltages

$$V = V_h - V_s \tag{28}$$

From eqn (25):

$$J_h = q\left[J_{e,diff}(0,T) + J_{e,drift}(0,T)\right] = qN_0 \times\left\{D_h(T)\left[\frac{-Q_2(T)\{S_i(T)+D_h(T)Q_1(T)\}e^{\Delta d/2} + Q_1(T)\{S_i(T)+D_h(T)Q_2(T)\}e^{-\Delta d/2}}{\{S_i(T)+D_h(T)Q_1(T)\}e^{\Delta d/2} - \{S_i(T)+D_h(T)Q_2(T)\}e^{-\Delta d/2}}\right] + \mu_{ext}(T)E\right\} \times \left(\exp\left[\frac{\mu_e(T)V_h}{D_h(T)}\right] - 1\right) \tag{29}$$

Grouping terms for simplicity:

$$A \equiv qN_0 \tag{30a}$$

$$B \equiv D_h(T)\left[\frac{-Q_2(T)\{S_i(T)+D_h(T)Q_1(T)\}e^{\Delta d/2} + Q_1(T)\{S_i(T)+D_h(T)Q_2(T)\}e^{-\Delta d/2}}{\{S_i(T)+D_h(T)Q_1(T)\}e^{\Delta d/2} - \{S_i(T)+D_h(T)Q_2(T)\}e^{-\Delta d/2}}\right] \tag{30b}$$

$$C \equiv \mu_{ext}(T)E \tag{30c}$$

$$D \equiv \frac{\mu_{ext}(T)}{D_h(T)} \tag{30d}$$

Eqn (29) can be written as

$$J_h = A(B + C)[\exp(D_h V_h) - 1] \tag{31}$$

Similarly, for the reverse diode, using eqn (26) and the same symbols as above with the subscript (i)

$$J_s = A(B_i + C_i)[\exp(D_{hi} V_s) - 1] \tag{32}$$

From eqn (27b) and (32)

$$V_s = \frac{1}{D_i}\ln\left[\frac{J}{A(B_i + C_i)} + 1\right] \tag{33}$$

and from eqn (27a) and (31)

$$V_h = \frac{1}{D}\ln\left[\frac{J_{ph} - J}{A(B + C)} + 1\right] \tag{34}$$

Combining these expressions yields the circuit output voltage:

$$\begin{aligned} V(J,T) &= V_h - V_s \\ &= \frac{D_h(T)}{\mu_e(T)}\ln\left(\frac{J_{ph} - J}{A[B + \mu_{ext}(T)E]} + 1\right) \\ &\quad - \frac{D_{hi}(T)}{\mu_{ei}(T)}\ln\left(\frac{J}{A[B_i + \mu_{exti}(T)E_i]} + 1\right) \end{aligned} \tag{35}$$

4.3 Transport parameter measurements

Fig. 4 shows the measured open-circuit voltage and short-circuit current of the best solar cell in our sample as a function of temperature between 100 K and 300 K. The experimental *J–V* characteristics were fitted sequentially to the two-diode model of eqn (35). The results are shown in Fig. 3(b)–(f). In view of the fact that 11 unknown parameters (from Table 1) had to be extracted from five *J–V* curves at different temperatures, and in the absence of a rigorous mathematical proof of uniqueness of fit and measurement, two independent best-fitting computational programs were used to investigate the reliability and thus the uniqueness of the best-fitted results in a statistical analysis. These programs (mean-value best fit and statistical best fit) have been used successfully in earlier multi-parameter fits to experimental data from amorphous/crystalline silicon solar cell heterojunctions.[36] The full set of the best-fitted results using both methods is summarized in Table 1. It is seen that the results

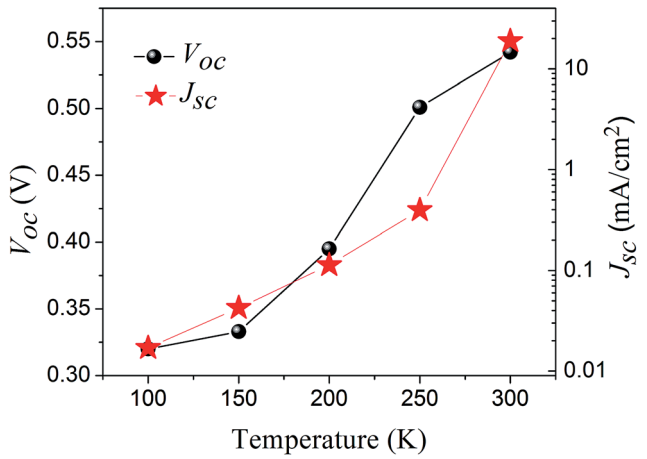

Fig. 4 Experimental open-circuit voltage (V_{oc}) and short-circuit current (I_{sc}) as a function of solar cell temperature.

from the two independent best-fitting programs are in very good-to-excellent agreement for all measured parameters, indicative of high reliability. Also, the statistical fit results show that variances were one order of magnitude smaller or less for all parameter measurements, indicative of high precision.

Table 1 also shows the extracted temperature dependence of the photocurrent density. The photocurrent density decrease with decreasing temperature is consistent with increased hole accumulation at the back interface and the subsequent strengthening of the reverse built-in electric field E_i which opposes further transport of holes toward the CQD–MoO_3 interface, thereby limiting the extracted solar cell current. Table 1 further shows the forward and reverse electric fields in the solar cell as functions of temperature. Although the non-monotonic behavior of E makes it hard to assert a general trend with decreasing temperature, the monotonically increasing trend of E_i is consistent with the foregoing interpretation of the concomitant decrease in photocurrent density. Table 1 also shows the calculated values of the hopping diffusion lengths of electrons and holes in the forward region and in the SCL. Although the statistical variances are relatively large, both diffusion lengths exhibit clearly non-monotonic behaviors. Given the definition, eqn (21), of $L_h(T)$, any interpretation of these trends would require the temperature behavior of the hopping diffusivity, $D_h(T)$ and that of the total (mean) electron and hole lifetime, $\tau(T)$, and $\tau_i(T)$, respectively. In view of the uncertainty in the exciton dissociation site, it is assumed that hole transport is mainly dominant in the SCL and electron transport mainly in the forward region. Fig. 5(a) shows the calculated $\tau(T)$ and, within the SCL, $\tau_i(T)$. Both hopping lifetimes are seen to decrease with increasing temperature. Although there exist no precedent measurements of the $\tau_i(T)$ and $\tau(T)$, these lifetime trends are in very good agreement with earlier frequency-domain photocarrier radiometry (PCR) studies of exciton lifetimes in the same coupled PbS–CQD matrix.[37] The mean lifetime in that material was found to decrease monotonically with increasing T and has significant temperature-dependent non-radiative and radiative relaxation components: the former decay channel is controlled by longitudinal optical (LO) phonon–exciton interactions which limit the radiative lifetime and luminescence photon flux throughout the entire 100–300 K temperature range. On comparing the dynamic PCR mean lifetime values in the materials (ref. 37, Table 1) with the static values extracted from the present J–V measurements through the developed transport theory of hopping particles in the complete solar cell fabricated from the same material matrix, it is seen that the trends are similar, however, the solar cell $\tau(T)$ values are consistently shorter than those of the materials alone (for example, 1.2 μs *vs.* 5.66–5.85 μs at 100 K). This is not surprising in view of possibly different exciton dissociation probabilities in the complete solar cell and is consistent with the increased hopping velocity (and mobility) of charge carriers contributing to the transit time across the body of the nanolayer in the presence of the drift-inducing electric field E, compared with that of the CQD material with $E = 0$, as predicted by eqn (6) with the (+) sign for transport in the direction of E. In Fig. 5(a) it is also observed that the $\tau_i(T)$ values within the temperature-variable SCL width W (see Table 1) under the opposing built-in electric field E_i are consistently longer than those of $\tau(T)$, in agreement with the decreasing hopping velocity, eqn (6) with the (−) sign. The two lifetimes converge to the same value at room temperature, an indication that hole accumulation at the interface becomes negligible and does not affect the transit time.

Increasing values of the hopping diffusivities $D_h(T)$ and $D_{hi}(T)$ with increasing temperature were also found from the best fits and are shown in Fig. 5(b). The trends are physically expected from diminishing resistance to hole transport as a result of decreased hole accumulation at the CQD–MoO_3 interface and increasing hopping frequency with increasing thermal energy content in the solid matrix. Specifically, eqn (9) shows that $D_h(T)$ can increase with temperature if the total carrier relaxation time $\tau(T)$ decreases.

Returning to Table 1, the non-monotonic trend in the values of $L_h(T)$ with increasing temperature can be easily understood to be due to the trade-off between decreasing mean carrier lifetime and increasing hopping diffusivity. From eqn (9) and (12), the opposing trends are between decreasing lifetime and increasing inter-dot hopping frequency which ultimately dominates at high temperatures thereby increasing L_h for $T > T_{min} = 200$ K of the L_h *vs.* T curve:

$$L_h(T) = L\sqrt{\frac{\tau(T)}{\tau_h(T)}} = L\sqrt{\frac{\tau(T)}{\tau_0}}\exp\left(-\frac{\Delta E}{2kT}\right) \qquad (36)$$

Inside the SCL, the opposite trends attributed to hole accumulation, are evident. The decrease in mean lifetime τ_i is much steeper, Fig. 5(a), possibly due to enhanced hole-to-hole scattering within the accumulation layer, and tends to offset any diffusion length increases due to hopping frequency increases. The net result is a decrease in L_{hi} for $T > T_{max} = 150$ K in the L_{hi} *vs.* T curve. At room temperature, although the decrease in L_{hi} probably has little effect on the overall transit time across the solar cell as hole accumulation diminishes, the overall net

Table 1 Summary of best-fitted results using both mean-value and statistical fitting methods

		Temperature, K									
		300		250		200		150		100	
Fitted parameters		Mean-value best fit	Statistical fit	Mean-value best fit	Statistical fit	Mean-value best fit	Statistical fit	Mean-value best fit	Statistical fit	Mean-value best fit	Statistical fit
Electron hopping diffusivity	D_h ($cm^2 s^{-1}$)	1.140×10^{-3}	$1.120 \times 10^{-3} \pm 2.534 \times 10^{-5}$	7.102×10^{-4}	$7.007 \times 10^{-4} \pm 2.539 \times 10^{-5}$	3.312×10^{-4}	$3.425 \times 10^{-4} \pm 2.232 \times 10^{-5}$	2.119×10^{-4}	$2.181 \times 10^{-4} \pm 6.583 \times 10^{-6}$	1.171×10^{-4}	$1.178 \times 10^{-4} \pm 6.335 \times 10^{-6}$
Electron hopping diffusion length	L_h (cm)	7.504×10^{-6}	$1.073 \times 10^{-5} \pm 3.230 \times 10^{-6}$	8.493×10^{-6}	$7.162 \times 10^{-6} \pm 1.334 \times 10^{-6}$	6.742×10^{-6}	$5.655 \times 10^{-6} \pm 1.094 \times 10^{-6}$	8.735×10^{-6}	$8.292 \times 10^{-6} \pm 9.687 \times 10^{-7}$	1.270×10^{-5}	$1.174 \times 10^{-5} \pm 1.533 \times 10^{-6}$
Electron hopping mobility	μ_e ($cm^2 V^{-1} s^{-1}$)	5.640×10^{-3}	$5.830 \times 10^{-3} \pm 1.930 \times 10^{-4}$	2.770×10^{-3}	$2.890 \times 10^{-3} \pm 1.244 \times 10^{-4}$	1.710×10^{-3}	$1.650 \times 10^{-3} \pm 9.052 \times 10^{-5}$	9.119×10^{-4}	$9.095 \times 10^{-4} \pm 4.261 \times 10^{-5}$	3.460×10^{-4}	$3.634 \times 10^{-4} \pm 1.765 \times 10^{-5}$
Electric field across the film	E ($V cm^{-1}$)	2.938×10^{5}	$2.966 \times 10^{5} \pm 1.434 \times 10^{4}$	3.942×10^{5}	$3.702 \times 10^{5} \pm 2.416 \times 10^{4}$	4.386×10^{5}	$4.260 \times 10^{5} \pm 2.071 \times 10^{4}$	2.704×10^{5}	$3.007 \times 10^{5} \pm 3.120 \times 10^{4}$	3.905×10^{5}	$3.915 \times 10^{5} \pm 3.033 \times 10^{4}$
Hole hopping diffusivity	D_{hi} ($cm^2 s^{-1}$)	8.109×10^{-4}	$7.561 \times 10^{-4} \pm 5.577 \times 10^{-5}$	4.305×10^{-4}	$4.350 \times 10^{-4} \pm 2.680 \times 10^{-5}$	1.410×10^{-4}	$1.387 \times 10^{-4} \pm 1.009 \times 10^{-5}$	6.131×10^{-5}	$6.547 \times 10^{-5} \pm 4.279 \times 10^{-6}$	3.004×10^{-5}	$3.081 \times 10^{-5} \pm 1.449 \times 10^{-6}$
Hole hopping diffusion length	L_{hi} (cm)	3.742×10^{-6}	$3.797 \times 10^{-6} \pm 1.968 \times 10^{-7}$	6.412×10^{-6}	$5.617 \times 10^{-6} \pm 9.404 \times 10^{-7}$	1.043×10^{-5}	$1.040 \times 10^{-5} \pm 1.472 \times 10^{-6}$	1.258×10^{-5}	$1.190 \times 10^{-5} \pm 1.322 \times 10^{-6}$	1.098×10^{-5}	$1.051 \times 10^{-5} \pm 1.147 \times 10^{-6}$
Local space charge layer	W (cm)	2.003×10^{-5}	$1.998 \times 10^{-5} \pm 2.608 \times 10^{-7}$	1.633×10^{-5}	$1.613 \times 10^{-5} \pm 6.165 \times 10^{-7}$	1.300×10^{-5}	$1.336 \times 10^{-5} \pm 8.316 \times 10^{-7}$	1.179×10^{-5}	$1.173 \times 10^{-5} \pm 7.204 \times 10^{-7}$	1.113×10^{-5}	$1.095 \times 10^{-5} \pm 3.616 \times 10^{-7}$
Local electric filed	E_i ($V cm^{-1}$)	2.127×10^{5}	$1.792 \times 10^{5} \pm 4.001 \times 10^{4}$	1.758×10^{5}	$1.798 \times 10^{5} \pm 1.215 \times 10^{4}$	1.947×10^{5}	$1.814 \times 10^{5} \pm 1.671 \times 10^{4}$	2.377×10^{5}	$2.372 \times 10^{5} \pm 2.042 \times 10^{4}$	2.889×10^{5}	$3.081 \times 10^{5} \pm 2.504 \times 10^{4}$
Photocurrent density	J_{ph} ($mA cm^{-2}$)	18.429	19.286 ± 1.412	6.239	6.719 ± 0.486	5.273	4.970 ± 0.310	3.274	3.146 ± 0.165	1.224	1.282 ± 0.087
Hole hopping mobility	μ_{ei} ($cm^2 V^{-1} s^{-1}$)	4.27×10^{-3}	$4.24 \times 10^{-3} \pm 9.8247 \times 10^{-5}$	9.697×10^{-4}	$9.743 \times 10^{-4} \pm 5.928 \times 10^{-5}$	3.468×10^{-4}	$3.425 \times 10^{-4} \pm 2.470 \times 10^{-5}$	7.982×10^{-5}	$8.531 \times 10^{-5} \pm 5.524 \times 10^{-6}$	2.822×10^{-5}	$2.899 \times 10^{-5} \pm 1.421 \times 10^{-6}$
Surface recombination velocity	SRV ($cm s^{-1}$)	9.628×10^{5}	$9.676 \times 10^{5} \pm 5.419 \times 10^{3}$	1.974×10^{3}	$8.232 \times 10^{3} \pm 7.194 \times 10^{3}$	4.172×10^{3}	$1.526 \times 10^{4} \pm 1.448 \times 10^{4}$	7.945×10^{3}	$4.659 \times 10^{3} \pm 3.302 \times 10^{3}$	6.546×10^{2}	$1.118 \times 10^{4} \pm 1.186 \times 10^{4}$

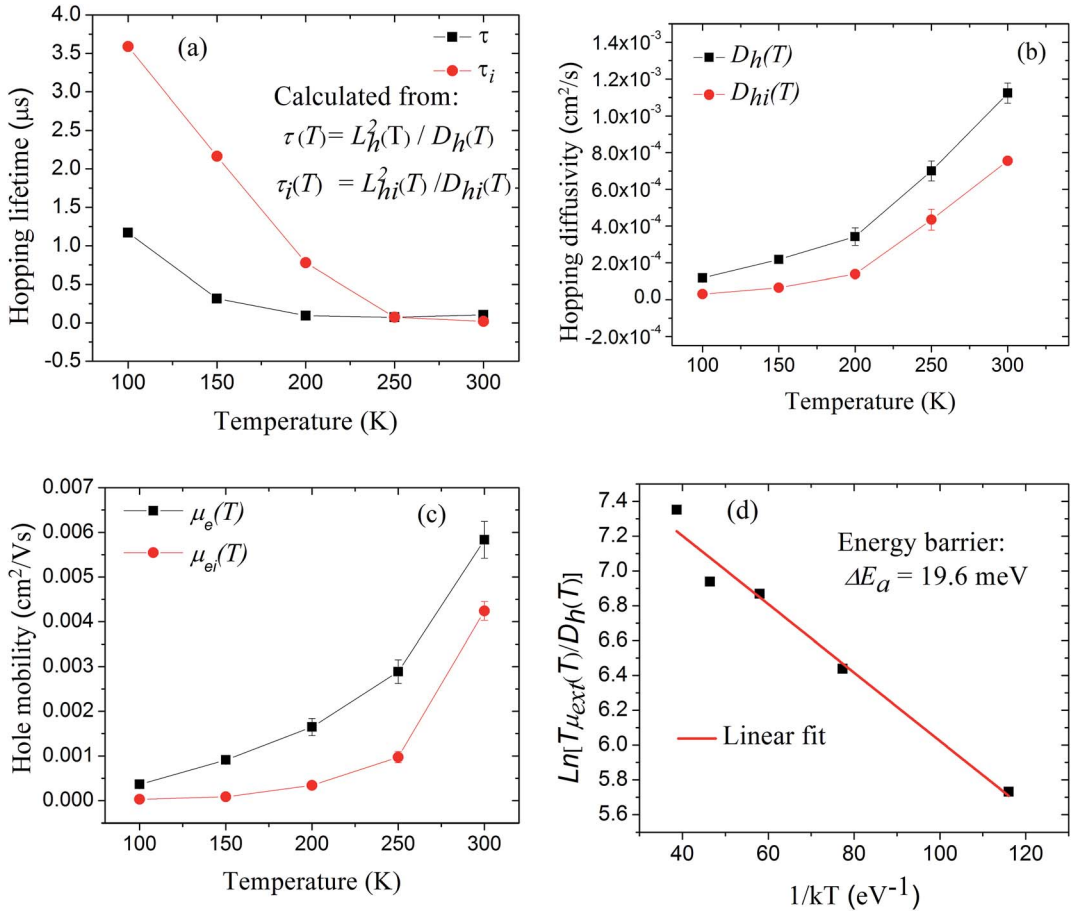

Fig. 5 (a) Total extracted hopping lifetimes for forward and reverse diodes, corresponding to electrons and holes. (b) Extracted hopping diffusivity *vs.* temperature in the forward region and in the SCL. (c) Extracted hopping mobility *vs.* temperature in the forward region and in the SCL. (d) Arrhenius plot of the ratio $T\mu_{ext}(T)/D_h(T)$ proving the validity of the modified Einstein eqn (14).

diffusion length is smaller than L_h which controls the carrier transport within the forward region of the solar cell. Upon dissociation, this decreases the hole crossing rate, in addition to the Schottky barrier at the CQD–MoO_3 interface.

Fig. 5(c) shows the extracted electron and hole mobilities in the two regions. They both increase with increasing temperature and the room-T values are in agreement with those obtained experimentally for PbS CQD.[5,38] Electron mobility, μ_e, has been reported to increase with temperature in a quantum dot superlattice.[39] Other reports[40,41] show that in semiconductor nanocrystal solids and PbSe quantum dots, device current increases with temperature which is indicative of a concomitant μ_e increase. Eqn (9) and (11a) show that the hopping diffusivity is dominated by inter-quantum dot hopping, and is the result of hopping attempts with activation energy ΔE. Eqn (13b) shows that the mobility, in addition to inter-quantum-dot hopping, is further limited by the reverse Schottky barrier height E_a. Therefore, separate measurements of diffusivity and mobility can yield information about these activation energies. Based on eqn (12), Fig. 6(a) is an Arrhenius plot of the product $[T\mu_{ext}(T)]$ and demonstrates the thermal activation nature of the transport across the solar cell layer with effective activation energy E_a = 49.9 meV. Fig. 5(d) is an Arrhenius plot of $[T\mu_{ext}(T)/D_h(T)]$, a combination of terms identified in eqn (14) which replaces the conventional Einstein relation in the CQD hopping transport theory. The figure experimentally proves the validity of the new hopping Einstein relation and extracts an effective barrier activation energy ΔE_a = 19.6 meV. The slopes of the curves in Fig. 6(a) and 5(d) can be used to deduce the hopping dot-to-dot energy barrier value ΔE = 30.3 meV. Furthermore, an Arrhenius plot of the hopping diffusivity, Fig. 6(b), yields ΔE = 27.6 meV, in very good agreement with the value obtained from the hopping Einstein relation. The experimentally extracted monotonic mobility increase with temperature is in agreement with earlier theoretical mobility calculations consistent with a hopping mechanism.[22] Both the present and the earlier trends are opposite from the expected mobility behavior for band-like conduction, where conventional photocarrier transport theory[28] predicts increasing mobility with decreasing temperature. The activation energy range for mobilities in CdSe[42] and PbSe[43] CQDs was found to be 10–50 meV, consistent with our calculated value in PbS CQD solar cells which, however, includes the additional Schottky barrier contribution at the CQD–metal interface.

Inside the SCL, similar calculations using the data in Fig. 5(b) and (c) and 6(c), and constructing Arrhenius plots for

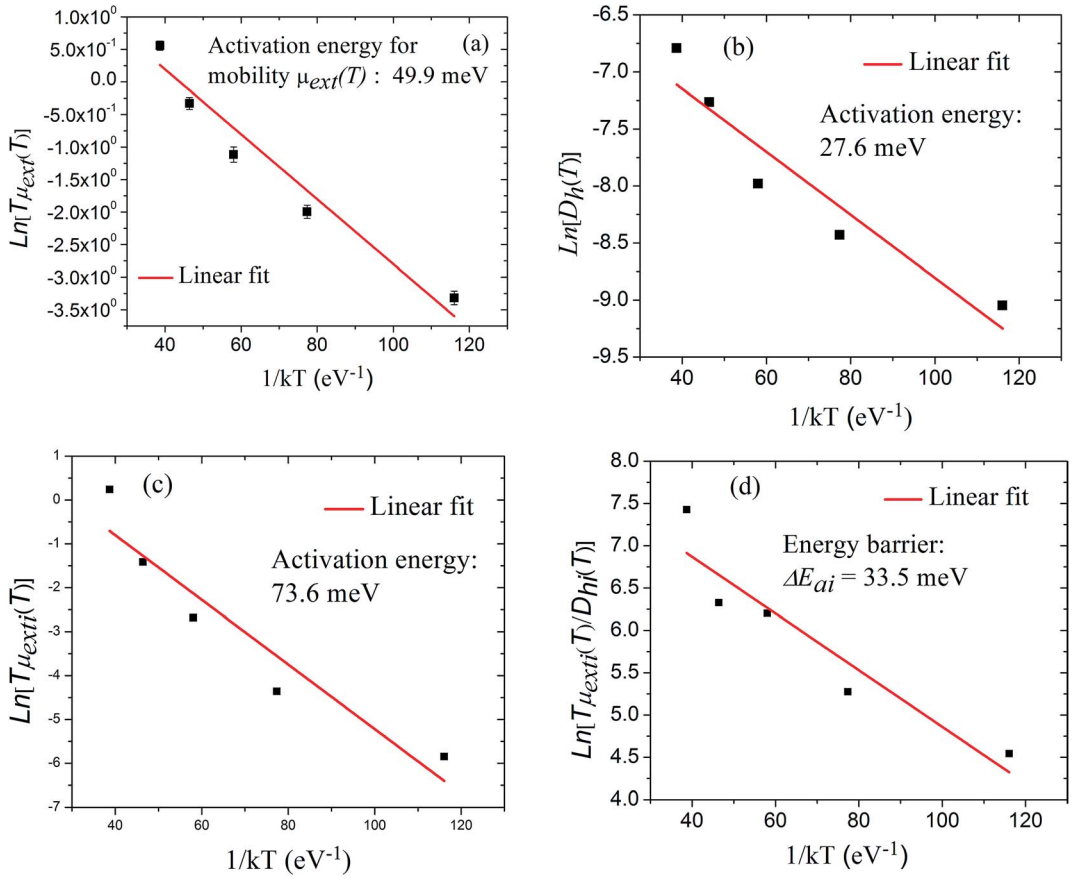

Fig. 6 (a) Arrhenius plot of hopping mobility to extract the effective activation energy $E_{\text{eff}} = E_a + \Delta E_a$. (b) Arrhenius plot of Fig. 5(b)–(d) are Arrhenius plots of the ratio $T\mu_{\text{ext}i}(T)$ and $T\mu_{\text{ext}i}(T)/D_{\text{h}i}(T)$, respectively.

$[T\mu_{\text{ext}i}(T)]$ and $[T\mu_{\text{ext}i}(T)/D_{\text{h}i}(T)]$, Fig. 6(c) and (d), gave $E_{ai} = 73.6$ meV and $\Delta E_{ai} = 33.5$ meV, respectively. The Arrhenius plot of the hopping diffusivity inside the SCL yielded $E_{ai} = 40.1$ meV. These values are significantly higher than those obtained from the current densities outside the SCL. The calculated dot-to-dot energy barrier $\Delta E_i = 40.1$ meV, higher than $\Delta E = 30.3$ meV in the CQD bulk, is consistent with holes forced to transition to higher energy levels in neighboring QDs due to the higher density of available holes already occupying lower levels.[27] The higher local-electric-field-induced barrier height ΔE_{ai} is also consistent with the presence of the local built-in electric field opposing the transport of holes across the SCL, Fig. 2(b) and (c), and preventing them from reaching the interface, a sort of reverse bias within the framework of hopping conduction.

The SCL width W dependence on temperature was also calculated from the best-fits to eqn (35) and the results are shown in Table 1. The increase in W with increasing temperature is consistent with the simultaneously occurring decrease in accumulated hole density at the PbS CQD/MoO_3 interface which appears to act as a conventional junction depletion layer: at low temperatures a large density of carriers (holes), Fig. 2(c), accumulated due to low interface recombination velocities (here S_i plays the role of extraction, rather than recombination, rate) is tantamount to a high local doping density, resulting in a high density of occupied local QD energy states, and therefore a narrow depletion layer and a strong reverse "built-in" electric field E_i. As temperature increases, the carrier density at the interface decreases as the higher diffusivity, and increased extraction rate S_i (this was only proven reliably and quantitatively for the $T = 300$ K case, Table 1), alleviate the concentration gradient, resulting in decreased density of occupied local QD energy states, therefore a wider depletion layer, and weaker reverse built-in electric field, Fig. 2(b). A theoretical expression for S_i in terms of local transport parameters can be obtained using eqn (7) evaluated at $x = d$:

$$J_{ei}(d,T) = -D_{\text{h}i}(T)\left.\frac{\mathrm{d}N_{\text{PV}}(x)}{\mathrm{d}x}\right|_{x=d} + \mu_{\text{ext}i}(T)E_iN_{\text{PV}}(d) \qquad (37)$$

When there is no net flux of carriers out of the interface, setting $J_{ei}(d,T) = 0$ and using eqn (22) yields

$$S_i(T) \equiv -\mu_{\text{ext}i}(T)E_i = \mu_{\text{ext}i}(T)|E_i| \qquad (38)$$

This expression of the SRV involves the value of the mobility at the interface and it is positive because the direction of the local built-in electric field vector is negative. The hopping mobility increases with T whereas E_i decreases. These opposite trends determine whether the net hole extraction rate across the junction depletes or accumulates the hole density within the

SCL. Table 1 shows that W covers the entire thickness range of the solar cell at 300 K. This allows the spreading of accumulated holes across the PbS CQD nanolayer and the minimization of the hole repelling electric field E_i at the MoO_3 interface, thereby largely restoring the solar cell J–V characteristics to the conventional exponential behavior, Fig. 3(b)–(f), while the barrier remains.

Fig. 7 shows the connection of the foregoing hole accumulation process within the SCL to the observed temperature dependence of V_{oc}, Fig. 4. With decreasing temperature, the hole extraction rate, S_i, decreases while the reverse drift current density $J_{ei,drift}$, eqn (26b), increases, thereby decreasing the net forward drift flux to the PbS CQD/MoO_3 interface. The net diffusion current density $J_{e,diff}$ is not affected by E_i, so the net forward transport rate is impeded. The changes in both interface depletion (out-diffusion, extraction, R_o) and accumulation (in-diffusion, R_i) rates within the SCL favor hole accumulation at the anode, provided $R_i > R_o$, thereby reducing the work function of the anode and leading to reduced V_{oc} (ref. 8) as observed in Fig. 4. This is the hopping conduction analog of conventional inorganic solar cell quasi Fermi level rise when holes accumulate near the anode metal at low temperatures, resulting in perturbation of the electron cloud distribution in the metal and V_{oc} decrease. The process comparing 200 K and 300 K energy diagrams using data from our measurements is shown in Fig. 7.

The similarities to a conventional depletion junction interface (with an exceedingly small depletion width on the other side of the junction due to the very high density of states in MoO_3) can be exploited in solar cell design optimization. The use of a high-work-function metal for minimizing the hole-injection barrier seems to be only partly effective due to Fermi level pinning at the interface.[15] Therefore, additional improvements can be sought with the trans-QD transport rate such as optimizing the dot-to-dot distance: The structure of the hopping diffusivity and mobility eqn (9) and (10) suggests that these quantities can be maximized for mean distances $\langle L\rangle = \frac{2}{\gamma}$. The transmission coefficient γ can be estimated from quantum mechanical hopping theory:[44] $\gamma = 2[(2m_e\Delta E/q)^{1/2}\hbar]$, where $\Delta E/q$ is the free exciton or dissociated carrier-to-dot barrier height and can be calculated from the Arrhenius plot of the measured diffusivity at several temperatures, Fig. 6(b). In addition, in view of the different values of the transport parameters within the SCL, a quantum dot ensemble adjacent to the metal interface with a mean dot-to-dot distance $\langle L_i\rangle = \frac{2}{\gamma_i}$ with $\gamma_i = 2[(2m_e\Delta E_i/q)^{1/2}\hbar]$ and ΔE_i calculated from an Arrhenius plot of the SCL diffusivity extracted from similar data, can result in overall optimized Schottky barrier which controls ΔE_i, thereby optimizing the hole transport rate across the CQD/metal interface by lowering the Schottky barrier using different interface (junction) conducting thin films.

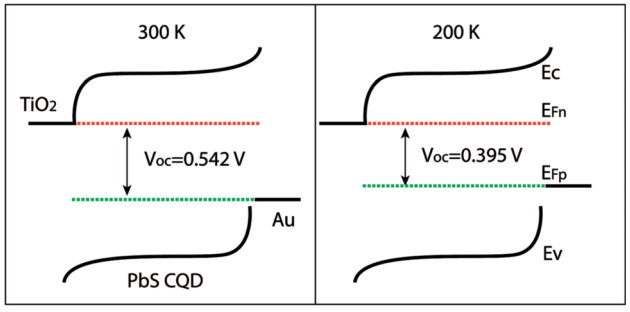

Fig. 7 Energy diagram showing the effects of temperatures (300 K and 200 K) on V_{oc}.

5 Conclusions

A theoretical model of charge carrier hopping transport across PbS CQD solar cells as a function of temperature was developed which led to hopping diffusion and drift components and analytical expressions for the carrier hopping diffusivity, velocity (hence, mobility), and a new hopping Einstein equation linking the latter two dynamic properties. The model was applied to a two-diode-equivalent optoelectronic configuration in order to explain experimental J–V curves obtained from glass/FTO/TiO_2/PbS QD/MoO_3/Au/Ag solar cells which exhibited anomalous characteristics at temperatures below 300 K (room temperature). Detailed best-fits of the J–V data to the theory over the 300–100 K temperature range were consistent with two transport regions within the solar cell, one forward, and the other a space charge layer associated with a reverse Schottky barrier. In each region, local parameters were measured using two best-fitting methods to ensure uniqueness of the results. Besides the physical insights, the model was found to be capable of estimating the optimal quantum dot-to-dot distance in CQD solar cells in order to maximize the hopping diffusivity and mobility, thereby improving solar power conversion efficiency.

Acknowledgements

The authors are grateful to the Natural Sciences and Engineering Research Council of Canada (NSERC) for a Discovery grant to AM, and the Canada Research Chairs program. AM gratefully acknowledges the Chinese Recruitment Program of Global Experts (Thousand Talents). He also acknowledges the Foundation for Innovative Research Groups of the National Natural Science Foundation of China (Grant No. 61421002). JW and LH gratefully acknowledge the China Scholarship Council (CSC) program. JW is also grateful to the National Natural Science Foundation of China (Grant No. 61379013). Sjoerd Hoogland and Edward H. Sargent are acknowledged for contributing CQD samples.

References

1 A. H. Ip, S. M. Thon, S. Hoogland, O. Voznyy, D. Zhitomirsky, R. Debnath, L. Levina, L. R. Rollny, G. H. Carey, A. Fischer, K. W. Kemp, I. J. Kramer, Z. Ning, A. J. Labelle, K. W. Chou, A. Amassian and E. H. Sargent, *Nat. Nanotechnol.*, 2012, 7(9), 577–582.

2 A. G. Pattantyus-Abraham, I. J. Kramer, A. R. Barkhouse, X. Wang, G. Konstantatos, R. Debnath, L. Levina, I. Raabe, M. K. Nazeeruddin, M. Grätzel and E. H. Sargent, *ACS Nano*, 2010, **4**, 3374–3380.
3 C. H. M. Chuang, P. R. Brown, V. Bulović and M. G. Bawendi, *Nat. Mater.*, 2014, **13**(8), 796–801.
4 C. H. M. Chuang, A. Maurano, R. E. Brandt, G. W. Hwang, J. Jean, T. Buonassisi, V. Bulovic and M. G. Bawendi, *Nano Lett.*, 2015, **15**(5), 3286–3294.
5 G. H. Carey, A. L. Abdelhady, Z. Ning, S. M. Thon, O. M. Bakr and E. H. Sargent, *Chem. Rev.*, 2015, **115**(23), 12732–12763.
6 D. K. Ko, P. R. Brown, M. G. Bawendi and V. Bulović, *Adv. Mater.*, 2014, **26**(28), 4845–4850.
7 J. C. Wang, X. C. Ren, S. Q. Shi, C. W. Leung and P. K. Chan, *Org. Electron.*, 2011, **12**(6), 880–885.
8 A. Wagenpfahl, D. Rauh, M. Binder, C. Deibel and V. S. Dyakonov, *Phys. Rev. B: Condens. Matter Mater. Phys.*, 2010, **82**(11), 115306.
9 L. Zuo, J. Yao, H. Li and H. Chen, *Sol. Energy Mater. Sol. Cells*, 2014, **122**, 88–93.
10 B. Romero, G. del Pozo, B. Arredondo, J. P. Reinhardt, M. Sessler and U. Wurfel, *IEEE Journal of Photovoltaics*, 2015, **5**(1), 234–237.
11 F. A. De Castro, J. Heier, F. Nüesch and R. Hany, *IEEE J. Sel. Top. Quantum Electron.*, 2010, **16**(6), 1690–1699.
12 D. Gupta, M. Bag and K. S. Narayan, *Appl. Phys. Lett.*, 2008, **92**(9), 093301.
13 A. Kumar, S. Sista and Y. Yang, *J. Appl. Phys.*, 2009, **105**, 094512.
14 W. Tress, A. Petrich, M. Hummert, M. Hein, K. Leo and M. Riede, *Appl. Phys. Lett.*, 2011, **98**(6), 063301.
15 J. Gao, J. M. Luther, O. E. Semonin, R. J. Ellingson, A. J. Nozik and M. C. Beard, *Nano Lett.*, 2011, **11**, 1002–1008.
16 M. Wolf and H. Rauschenbach, *Adv. Energy Convers.*, 1963, **3**(2), 455–479.
17 P. Granero, V. S. Balderrama, J. Ferre-Borrull, J. Pallares and L. F. Marsal, *J. Appl. Phys.*, 2013, **113**, 043107.
18 L. A. A. Pettersson, L. S. Roman and O. Inganas, *J. Appl. Phys.*, 1999, **86**(1), 487–496.
19 T. Stubinger and W. Brutting, *J. Appl. Phys.*, 2001, **90**(7), 3632–3641.
20 D. Zhitomirsky, O. Voznyy, S. Hoogland and E. H. Sargent, *ACS Nano*, 2013, **7**(6), 5282–5290.
21 A. Lagendijk, B. van Tiggelen and D. S. Wiersma, 50 Years of Anderson Localization, *Phys. Today*, 2009, **62**, 24–29.
22 P. Guyot-Sionnest, *J. Phys. Chem. Lett.*, 2012, **3**, 1169–1175.
23 J. Wang and A. Mandelis, *J. Phys. Chem. C*, 2014, **118**, 19484–19491.
24 B. D. Gerardot, S. Seidl, P. A. Dalgarno, R. J. Warburton, D. Granados, J. M. Garcia, K. Kowalik, O. Krebs, K. Karrai, A. Badolato and P. M. Petroff, *Appl. Phys. Lett.*, 2007, **90**, 041101.
25 A. J. Bennett, M. A. Pooley, R. M. Stevenson, M. B. Ward, R. B. Patel, A. B. de La Giroday, N. Sköld, I. Farrer, C. A. Nicoll, D. A. Ritchie and A. J. Shields, *Nat. Phys.*, 2010, **6**(12), 947–950.
26 G. Hönig, S. Rodt, G. Callsen, I. A. Ostapenko, T. Kure, A. Schliwa, C. Kindel, D. Bimberg, A. Hoffmann, S. Kako and Y. Arakawa, *Phys. Rev. B: Condens. Matter Mater. Phys.*, 2013, **88**(4), 045309.
27 H. E. Roman and L. Pavesi, *J. Phys.: Condens. Matter*, 1996, **8**, 5161–5187.
28 J. P. McKelvey, *Solid State and Semiconductor Physics*, Harper and Row, New York, 1969.
29 D. S. Ginger and N. C. Greenham, *J. Appl. Phys.*, 2000, **87**, 1361–1368.
30 J. Gao, J. Zhang, J. van de Lagemaat, J. C. Johnson and M. C. Beard, *ACS Nano*, 2014, **8**, 12814–12825.
31 K. Kanai, K. Koizumi, S. Ouchi, Y. Tsukamoto, K. Sakanoue, Y. Ouchi and K. Seki, *Org. Electron.*, 2010, **11**(2), 188–194.
32 I. Hancox, P. Sullivan, K. V. Chauhan, N. Beaumont, L. A. Rochford, R. A. Hatton and T. S. Jones, *Org. Electron.*, 2010, **11**(12), 2019–2025.
33 J. Meyer, A. Shu, M. Kroger and A. Kahn, *Appl. Phys. Lett.*, 2010, **96**(13), 133308.
34 Irfan, H. Ding, Y. Gao, C. Small, D. Y. Kim, J. Subbiah and F. So, *Appl. Phys. Lett.*, 2010, **96**, 243307.
35 V. V. Eremenko, V. A. Karachevisev and V. V. Slavin, *Chem. Phys.*, 1997, **216**(1), 1–6.
36 Y. Zhang, A. Melnikov, A. Mandelis, B. Halliop, N. P. Kherani and R. Zhu, *Rev. Sci. Instrum.*, 2015, **86**, 033901.
37 J. Wang, A. Mandelis, A. Melnikov, S. Hoogland and E. H. Sargent, *J. Phys. Chem. C*, 2013, **117**(44), 23333–23348.
38 J. Tang and E. H. Sargent, *Adv. Mater.*, 2011, **23**(1), 12–29.
39 S. Xu, D. Thian, S. Wang, Y. Wang and F. B. Prinz, *Phys. Rev. B: Condens. Matter Mater. Phys.*, 2014, **90**(14), 144202.
40 D. Yu, C. Wang, B. L. Wehrenberg and P. Guyot-Sionnest, *Phys. Rev. Lett.*, 2004, **92**(21), 216802.
41 H. E. Romero and M. Drndic, *Phys. Rev. Lett.*, 2005, **95**(15), 156801.
42 D. Yu, C. J. Wang and P. Guyot-Sionnest, *Science*, 2003, **300**(5623), 1277–1280.
43 Y. Liu, M. Gibbs, J. Puthussery, S. Gaik, R. Ihly, H. W. Hillhouse and M. Law, *Nano Lett.*, 2010, **10**, 1960–1969.
44 N. Kasamatsu, T. Kada, A. Hasegawa, Y. Harada and T. Kita, *J. Appl. Phys.*, 2014, **115**(8), 083510.